


Article

Effect of Trace La on Microstructure and Thermal Conductivity of Hypoeutectic Al-7Si Alloy

Jun-Yu Yue ^{1,2,†}, Ji-Cheng Li ^{3,†}, Yi Sui ^{1,4,*}, Lei Wen ³ and Rui-Ying Zhang ^{3,*} 

¹ State Key Laboratory of Baiyunobo Rare Earth Resource Researches and Comprehensive Utilization, Baotou Research Institute of Rare Earths, Baotou 014030, China; yuejunyu@brire.com

² School of Metallurgy, Northeastern University, Shenyang 110004, China

³ School of Materials Science and Engineering, Inner Mongolia University of Technology, Hohhot 010051, China; lj3137@163.com (J.-C.L.); wenlei202304@163.com (L.W.)

⁴ Hangzhou Baogang Rare Earth Technology Development Co., Ltd., Hangzhou 310000, China

* Correspondence: btsuiyi@126.com (Y.S.); zhang_ruiying@126.com (R.-Y.Z.)

† These authors contributed equally to this work.

Abstract

Al-Si phase change materials are widely used in solar thermal power generation and industrial waste heat reclamation due to their high heat storage density, high phase transition temperature, and low cost. Hypoeutectic Al-7Si phase change thermal storage alloys with trace La additions were produced through smelting and casting to examine how La affects their microstructural characteristics and thermophysical performance. The findings show that La is adsorbed at the eutectic Si growth interface. Due to the difference in atomic radii, it alters the stacking sequence of Si atoms, generating numerous high-density staggered twins on the {111}Si planes of eutectic Si. La additions modify the morphology of eutectic Si, leading to a morphological transition from lamellar to short rods structures with reduced dimensions. The optimal eutectic Si modification is achieved with 0.06 wt.% La addition. The altered morphology and reduced size of the eutectic Si phase enhance the continuity of the α -Al matrix. This reduces the scattering of free electrons by eutectic Si, increases their mean free path, and ultimately improves the thermal conductivity of the alloy. With 0.06 wt.% La addition, the Al-7Si alloy achieved a peak thermal conductivity of $179.3 \text{ W} \cdot \text{m}^{-1} \cdot \text{K}^{-1}$, representing a 15.36% enhancement over the unmodified alloy. After 100 thermal cycles, the alloy maintained its phase transition temperature, but the modification effect of La diminished, as evidenced by increased formation of lamellar eutectic Si. Consequently, the latent heat of the Al-7Si-0.06 alloy decreased from 340.4 J/g to 328.6 J/g.

Keywords: Al-Si alloy; phase change heat storage material; eutectic Si; high temperature oxidation resistance; rare-earth La



Academic Editor: Frank Czerwinski

Received: 31 August 2025

Revised: 26 September 2025

Accepted: 27 September 2025

Published: 29 September 2025

Citation: Yue, J.-Y.; Li, J.-C.; Sui, Y.; Wen, L.; Zhang, R.-Y. Effect of Trace La on Microstructure and Thermal Conductivity of Hypoeutectic Al-7Si Alloy. *Metals* **2025**, *15*, 1087. <https://doi.org/10.3390/met15101087>

Copyright: © 2025 by the authors. Licensee MDPI, Basel, Switzerland. This article is an open access article distributed under the terms and conditions of the Creative Commons Attribution (CC BY) license (<https://creativecommons.org/licenses/by/4.0/>).

1. Introduction

Al-based phase change thermal storage materials have promising application prospects in high-temperature thermal energy storage fields ($>250^\circ\text{C}$), such as solar thermal electricity generation and industrial waste heat application, owing to their relatively high phase transition temperatures (577°C) and substantial heat storage densities ($490\sim 510 \text{ J/g}$) [1–3]. Phase change thermal storage materials with higher thermal conductivity exhibit greater heat transfer rates within the storage container during thermal charging processes. This enhanced conductivity reduces flow resistance at the solid–liquid phase interface and accelerates melting rates, thereby improving the thermal response speed of the

energy storage system [4–6]. Bie et al. [7] found through comparative analysis of numerical simulation and experimental verification that when the thermal conductivity of the phase change material was increased threefold, its melting time was correspondingly reduced by 40%. Factors such as the decline in thermal storage performance of aluminum-based alloys after multiple melting and solidification thermal cycles, and the increase in oxidation rate under high-temperature environments, will limit the service life of the material in practical engineering applications [8–10]. Therefore, improving the thermal conductivity and thermal cycling stability of aluminum–silicon phase change thermal storage materials is a critical scientific issue that urgently needs to be addressed for the engineering application of thermal storage alloys.

The Wiedemann–Franz law [11] states that the Lorenz constant represents the ratio of thermal to electrical conductivity in alloys with free electrons mainly contributing to both conduction mechanisms. Resistivity differs significantly between phases in Al–Si alloy: the eutectic Si measures $2.14 \times 10^3 \Omega \cdot \text{m}$, while the primary α -Al phase is only $2.83 \times 10^{-8} \Omega \cdot \text{m}$. This increased resistivity more severely restricts electron flow relative to the primary α -Al phase. The same principle extends to thermal transport processes. During the smelting process of Al–Si alloy, coarse flake-like eutectic Si phases are formed. This microstructure severely damages the aluminum matrix, leading to marked degradation of thermal conductivity. Applying modification to Al–Si alloys transforms eutectic Si into finer structures, significantly increasing α -Al/eutectic Si phase boundary contact areas. Common modifying elements include Na [12], Sr [13,14], Sb [15], and B [13], as well as rare earth elements such as La [16,17], Ce [18], Y [19], and Eu [20]. Among them, rare earth elements are widely used as modifiers in Al–Si phase change thermal storage materials due to their unique physicochemical properties. In addition, the literature shows that high cooling rates and alternative alloying elements can refine/eliminate Si morphology [21–24]. Gan et al. [14] observed that Sr modification causes a morphological shift of eutectic Si from plate-like to fibrous structures within hypoeutectic Al–Si (3–12 wt.%) alloys. This change in eutectic Si morphology shortened free electron paths in lattice distortion zones, thereby improving thermal conductivity in the alloy. According to Zhu et al. [25], Er effectively refines Al–12Si alloy's primary Si phase. This refinement progressively improves thermal conductivity at higher Er contents. Chen et al. [26] employed dual Er/Sr (Er/Sr = 2:1, wt.%) modification in A356 alloy, inducing morphological evolution of eutectic Si from acicular to fibrous structures. Microstructural refinement enhanced the alloy's tensile strength by 10.7%. Studies have found that rare-earth La shows excellent refinement and modification effects on both primary α -Al and eutectic Si within Al–Si alloys [27–29]. Wu et al. [30] reported 26.8% grain refinement, 7.7% reduced secondary dendrite arm spacing, and 26.7% decreased area of eutectic Si within Al–7Si alloy containing 0.1 wt.% La. Jiang et al. [17] found that adding 0.2 wt.% RE (65 wt.% Ce and 35 wt.% La) resulted in uniform refinement of the eutectic Si in A357 alloy. The changes in the alloy's microstructure led to significant improvements in its tensile strength, yield strength, and elongation. Zheng et al. [27] observed that the addition of 0.06 wt.% La improved the grain structure of Al–6Si alloy, inducing multi-layer stacking faults and multiple twins in the eutectic Si, thereby enhancing its ductility. Pourbahari et al. [29] observed that 0.1 wt.% La modified AlSiMg alloy's eutectic Si morphology, forming Al_4La and AlSiLa intermetallic compounds, which improved the alloy's tensile properties. However, for Al–Si phase change thermal storage materials, current research has centered on how rare-earth La impacts the mechanical properties and microstructure of Al–Si alloy systems. Significantly less attention has been paid to the impacts of trace La on thermal conductivity and phase change latent heat.

Consequently, hypoeutectic Al–7Si alloy serves as the experimental matrix to examine the influence of trace La on microstructural evolution and solidification characteristics.

It aims to analyze the modification mechanism of La on the eutectic Si in Al-7Si alloy, investigate its impacts on thermal transport and latent heat characteristics, and engineer a phase change material with optimal heat storage performance.

2. Materials and Methods

2.1. Experimental Procedure

Al-7Si alloys with varying La content (0–0.1 wt.%) were fabricated using commercial purity aluminum (99.9%) combined with Al-20Si and Al-10La master alloys from Suzhou Haichuan Rare Metal Products Co., Ltd. (Suzhou, China). The experimental procedure was as follows: First, commercially pure aluminum (99.9%) and Al-20Si master alloy were loaded into a graphite–clay crucible preheated to 200 °C. The mixture was then heated to 750 °C using a resistance furnace (SG2-7.5-10) and held at this temperature for 1 h. A refining agent was subsequently added to degas and the slag was removed. Based on predetermined La concentrations, calculated amounts of Al-10La master alloy were sequentially introduced into the crucible. After the furnace temperature dropped to 720 °C, the mixture was held for 10 min, during which a graphite rod was used for stirring to ensure uniform alloy composition. Finally, the molten alloy was cast into a 200 °C-preheated steel permanent mold, yielding cylindrical specimens with dimensions of $\Phi 30 \text{ mm} \times 110 \text{ mm}$. Then, 20 g of alloy samples were weighed, placed in alumina crucibles, and subjected to thermal cycling experiments in a vacuum tube furnace. Based on the Al-Si binary phase diagram, to ensure complete melting and solidification of the alloys, the upper melting temperature and lower solidification temperature for thermal cycling were set 67 °C above and below the eutectic temperature, respectively. Thus, the thermal cycling temperature range for the six Al-7Si-xLa alloys was 510 °C to 644 °C. The thermal cycling procedure was carried out as follows: (1) The samples were heated to 700 °C and held for 30 min to ensure full melting, and then cooled to 510 °C and held for 30 min. (2) Thermal cycling was initiated by heating at a rate of 5 °C/min to 644 °C, held for 30 min, then cooled to 510 °C, and held for 30 min. One cycle consisted of heating from 510 °C to 644 °C and cooling back to 510 °C, and the experiment was conducted for 100 cycles. High-temperature oxidation resistance tests were conducted in a YTH-4-10 box furnace (Luoyang Kesote Furnace Industry Co., Ltd., Luoyang, China). Before the tests, the total mass of each alloy and its crucible was recorded. Crucibles containing the samples were neatly placed into the furnace chamber, with the test temperature set to 700 °C. After holding for 24 h, 48 h, 72 h, and 96 h, respectively, the samples were taken out, and the mass of each sample and its crucible was recorded. Oxidation kinetic curves were plotted using the weight gain method to evaluate the high-temperature oxidation resistance of the alloys.

2.2. Microstructural Characterization and Phase Analysis

The La content in the alloy was determined using inductively coupled plasma mass spectrometry (ICP-MS; PerkinElmer NexION 300Q, Waltham, MA, USA). The measurement was conducted in accordance with the Chinese National Standard GB/T 43589-2023 [31]: gold alloys for adornment—determination of multi-element contents by laser ablation–inductively coupled plasma mass spectrometry. Table 1 shows the actual measured results of La content in the alloy before and after thermal cycling. The alloy samples were ground and polished for microstructural characterization using optical microscopy to examine grain morphology and microdefects. To reveal the three-dimensional morphology of the eutectic Si phase, the polished samples were etched in a 10 wt% HCl solution for 30 min, ultrasonically cleaned, and subsequently observed under a scanning electron microscope (SEM; Zeiss Sigma 500, Carl Zeiss AG, Oberkochen, Germany). Elemental distribution mapping was performed via field emission electron probe microanalysis (EPMA; JAX-Ihp200F, JEOL, Tokyo, Japan).

Phase analysis employed a D/MAX2500V X-ray diffraction instrument (XRD) (Rigaku, Tokyo, Japan) using Cu K α radiation with the following scanning parameters: an angular range of 20° to 80° and a scan rate of 5°/min. A more in-depth analysis of the alloy's microstructure was conducted using a high-resolution transmission electron microscope (TEM, Talos F200i, Thermo Scientific, Waltham, MA, USA). A 10 mm \times 10 mm \times 1 mm alloy specimen was mechanically thinned to 80 μ m thickness. Subsequent ion milling was performed with a Gatan 695 precision polisher (Pleasanton, CA, USA) to prepare TEM-ready foils.

Table 1. Measured La concentrations in Al-7Si-xLa alloys before and after thermal cycling (wt.%).

Alloy	Al-7Si	Al-7Si-0.02La	Al-7Si-0.04La	Al-7Si-0.06La	Al-7Si-0.08La	Al-7Si-0.1La
As-cast (La content)	0.0010	0.022	0.038	0.058	0.075	0.090
Post-cycling (La content)	<0.0010	0.020	0.038	0.050	0.063	0.087

2.3. Heat Storage Performance Analysis

Phase transformation characteristics of the alloy were quantified via simultaneous thermal analysis (STA 449 F3), including onset and termination temperatures of phase change and associated latent heat. First, a cylindrical specimen (10 mg, precisely weighed) was loaded into an alumina crucible. Under the protection of a high-purity argon atmosphere, a symmetric thermal cycle was implemented with 5 °C/min ramping: heating from room temperature to 720 °C followed by cooling to room temperature at equivalent rate. The latent heat of phase transition was calculated using the analysis software integrated with the simultaneous thermal analyzer. Phase change enthalpy was quantified through numerical integration of the DSC fusion curve, where peak area directly corresponds to latent heat. Alloy density was determined via the Archimedes' principle buoyancy method using a DE-250ME electronic densitometer (Guangdong Hongtuo Instrument Technology Co., Ltd., Hongtuo, China). Thermophysical properties including thermal diffusivity (α) and specific heat capacity (C_p) were characterized at ambient temperature using a laser flash analyzer (LFA 467). The samples, sized 10 mm \times 10 mm \times 2 mm, were coated with a thin layer of thermally conductive graphite. The sample was placed into the instrument's heating chamber, and the thermal diffusivity and specific heat capacity were recorded once the measurements stabilized. Each sample was tested three times, and the average value was adopted to ensure accuracy. The instrument typically offers an accuracy better than $\pm 3\%$. Triplicate measurements ensured data accuracy, with mean values reported. Thermal conductivity (κ) was derived from Equation (1), where (ρ) denotes density.

$$\kappa = \alpha \cdot \rho \cdot C_p \quad (1)$$

3. Results and Discussion

3.1. Influence of Trace La on the Microstructure in Al-7Si Alloy

Figure 1 presents the metallographic structures and scanning electron micrographs of Al-7Si alloys containing varying La additions. Elemental distribution maps for Al-7Si alloys incorporating graded La concentrations are illustrated in Figure 2. Unmodified Al-7Si alloy (Figures 1a and 2a) exhibits a microstructure dominated by primary α -Al with lamellar eutectic Si. Eutectic Si primarily resides as coarse plate-like structures within the α -Al matrix. Adding 0.06 wt.% La modifies the eutectic Si morphology, transforming it from plate-like to short rod-like structures with a concurrent size reduction. Figures 1b and 2b demonstrate that La achieves optimal eutectic silicon refinement at this stage, transitioning its morphology from plates to short rods with significant size reduction. However, when

0.1 wt.% La is added, the number of plate-like eutectic Si phases within the alloy increases, though their size remains smaller than those in the unmodified Al-7Si alloy, as seen in Figures 1c and 2c. Figure 3 summarizes primary α -Al grain statistics across six sets of alloys. The unmodified Al-7Si alloy exhibits primary α -Al grains averaging 29.15 μm . As the La content increases, the grain size gradually decreases. Incorporating 0.06 wt.% La refines primary α -Al grains to 18.85 μm , achieving a 35.33% size reduction relative to the unmodified alloy. When 0.1 wt.% La is added, the α -Al grain size measures 22.22 μm , still smaller than that of the unmodified original alloy, reflecting a 23.77% reduction.

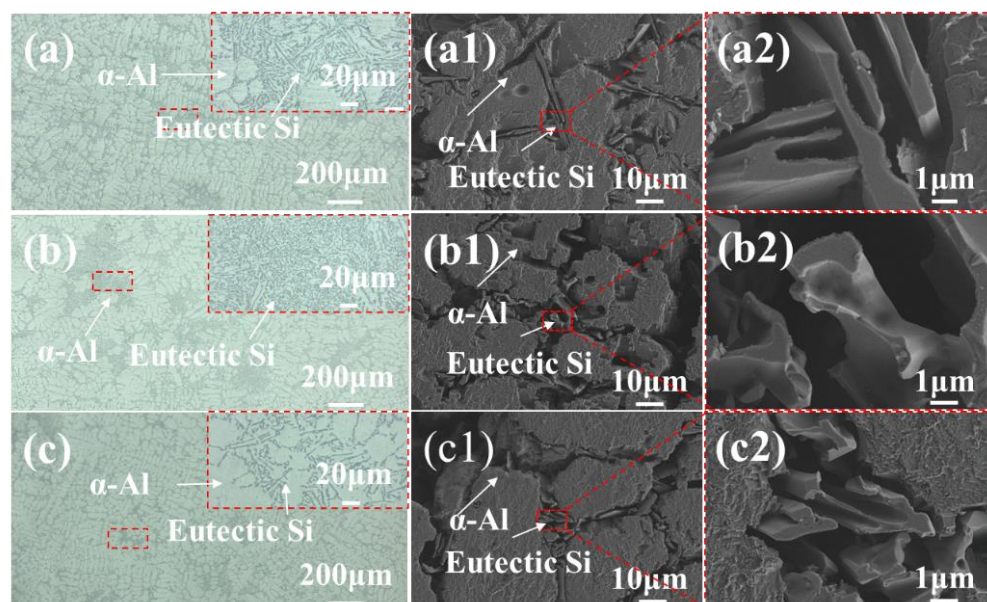


Figure 1. Microstructural characterization of Al-7Si alloys with different La additions: (a) Metallographic image of Al-7Si; (a1) SEM image of Al-7Si; (a2) Magnified view of (a1); (b) Metallographic image of Al-7Si-0.06La; (b1) SEM image of Al-7Si-0.06La; (b2) Magnified view of (b1); (c) Metallographic image of Al-7Si-0.1La; (c1) SEM image of Al-7Si-0.1La; (c2) Magnified view of (c1).

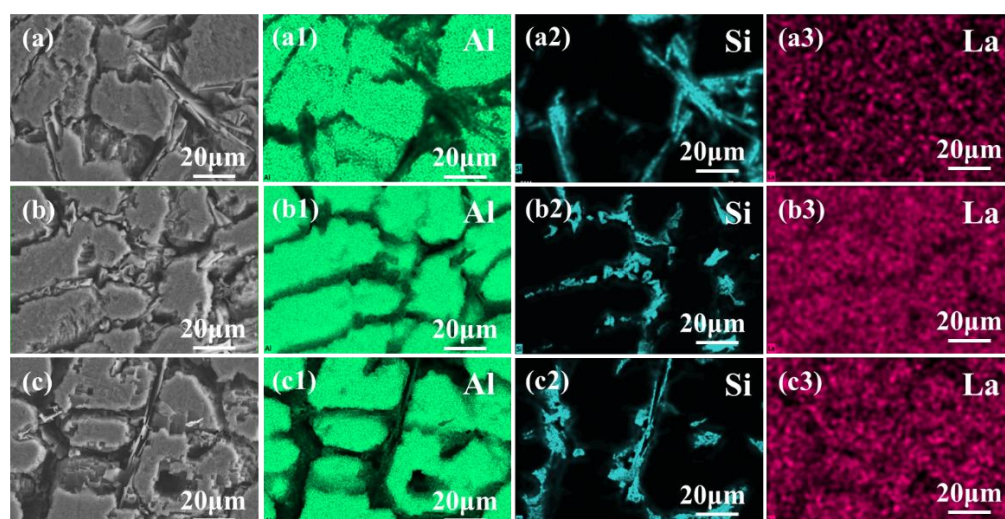


Figure 2. Energy-dispersive X-ray spectroscopy (EDS) analysis of Al-7Si alloys with varying La additions: (a) Al-7Si alloy; (a1) Al of Al-7Si alloy; (a2) Si of Al-7Si alloy; (a3) La of Al-7Si alloy; (b) Al-7Si-0.06La alloy; (b1) Al of Al-7Si-0.06La alloy; (b2) Si of Al-7Si-0.06La alloy; (b3) La of Al-7Si-0.06La alloy; (c) Al-7Si-0.1La alloy; (c1) Al of Al-7Si-0.1La alloy; (c2) Si of Al-7Si-0.1La alloy; (c3) La of Al-7Si-0.1La alloy.

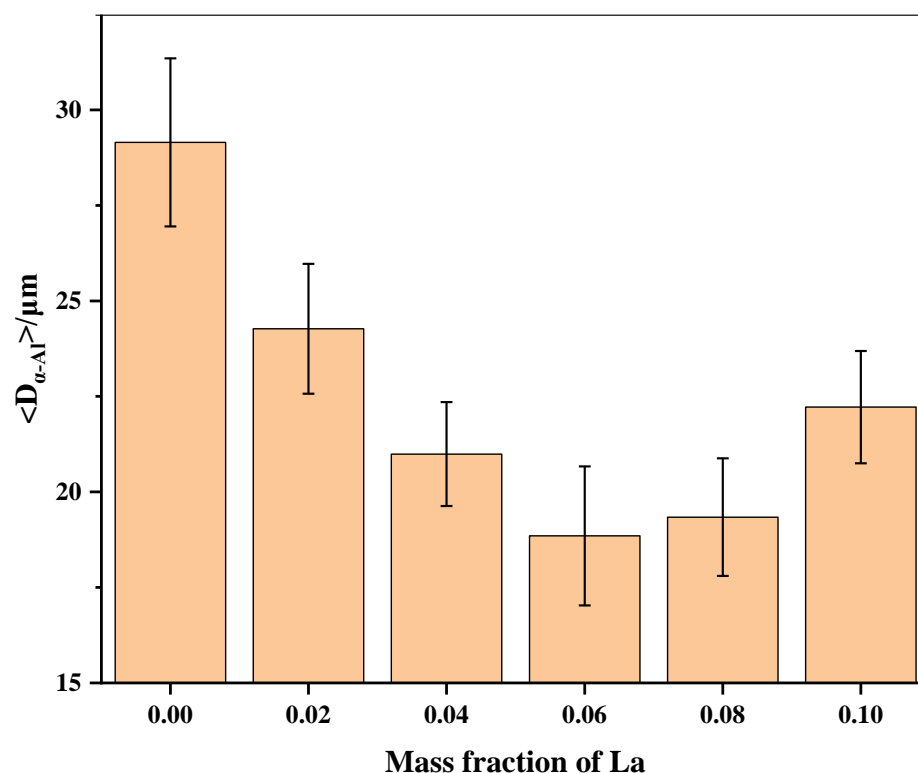


Figure 3. Grain size distribution of primary α -Al within Al-7Si alloys with different La additions.

Figure 4 shows a TEM bright-field micrograph and relevant selected-area electron diffraction (SAED) pattern of the unmodified Al-7Si alloy. Figure 4a shows the precipitation of plate-like eutectic Si phases from the α -Al matrix in the Al-Si eutectic reaction, with two distinct parallel Si plates clearly observable. Figure 4c,d demonstrate distinct twinning behaviors in the eutectic Si phases: one Si phase exhibits a twin-free surface with relatively large dimensions, while another Si phase contains low-density twins whose growth direction aligns with the primary growth direction of the eutectic Si. The calibration results of the electron diffraction pattern confirm that the $\{111\}$ Si plane functions as the twinning plane and the $\langle 112 \rangle$ Si direction serves as the twinning direction in eutectic silicon. Furthermore, step-like features are observed along the grain boundary (GB) separating eutectic Si and the α -Al matrix [32]. These interfacial steps, located at the solidification front (marked by red dotted lines in Figure 4d), can serve as preferential adsorption sites for modifying elements. The Al-7Si-0.06La alloy's TEM bright field micrograph along with the relevant SAED pattern are shown in Figure 5. Figure 5 demonstrates that trace La modification (0.06 wt.%) significantly refined the eutectic Si, transforming its morphology from plate-like to worm-like. Figure 5c presents the magnified view reveals that, unlike the unmodified alloy containing single-oriented parallel twins, the modified eutectic Si exhibits high-density twins with an inter-twin angle of 70.5° . The indexing results of the electron diffraction patterns confirm that the twin plane in eutectic Si remains the $\{111\}$ Si plane, with the twinning direction along $\langle 112 \rangle$ Si. The experimental results demonstrate that trace La additions to the Al-7Si alloy can induce the formation of high-density intersecting twins on eutectic Si surfaces, leading to significant refinement of Si particle size and morphological modification.

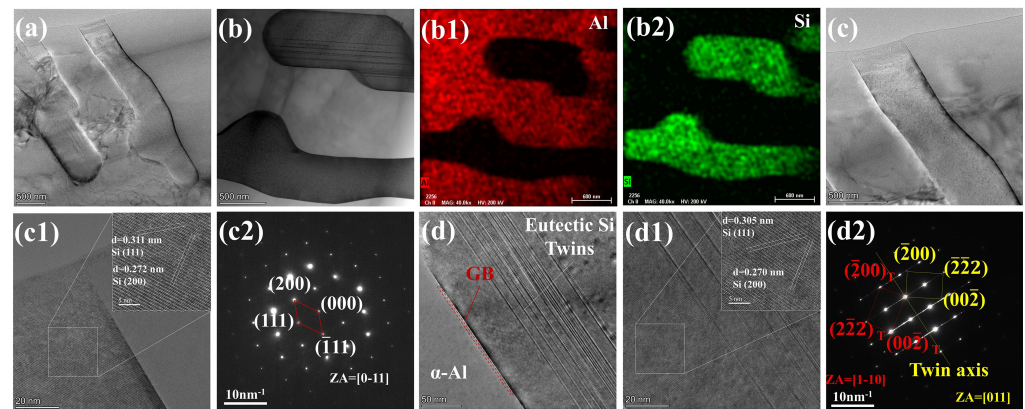


Figure 4. TEM micrographs of eutectic Si particles in Al-7Si alloy with corresponding SAED patterns: (a) microstructure of eutectic Si; (b) bright-field of TEM; (b1,b2): EDS; (c,d) magnification of eutectic Si particles; (c1,d1) high-resolution image of TEM; (c2,d2) SAED of (c1,d1).

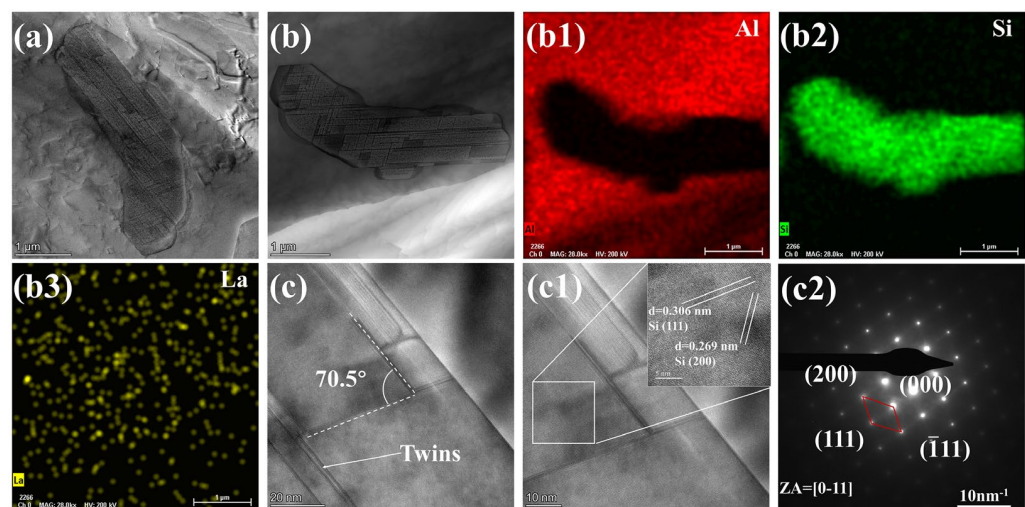


Figure 5. TEM micrographs of eutectic Si particles in Al-7Si-0.06La alloy with corresponding SAED patterns: (a) microstructure of eutectic Si; (b) bright-field of TEM; (b1–b3) EDS; (c) magnification of eutectic Si particles; (c1) high-resolution image of TEM; (c2) SAED of (c1).

This study found that rare earth elements tend to enrich near grain boundaries, leading to elemental segregation. Specifically, the trace addition of rare-earth La promotes the formation of rare-earth-rich phase particles. EPMA results indicate the formation of white compound particles near the eutectic Si phase. EDS elemental mapping identifies the bright microstructural features as La-enriched phase particles, as shown in Figure 6. XRD patterns for Al-7Si versus Al-7Si-0.06La alloys are presented in Figure 7. The original Al-7Si alloy exhibits diffraction peaks only from the α -Al phase (PDF#00-004-0787) and the eutectic Si phase (PDF#00-005-0565). At 0.06 wt.% La addition, the alloy maintains α -Al and eutectic silicon diffraction signatures while developing new peaks attributable to the AlSiLa phase (PDF#97-060-8329). Figure 8 characterizes rare-earth-bearing phases in Al-7Si-0.06La through TEM bright-field micrographs, EDS mapping, and SAED patterns. The results reveal the presence of lamellar rare earth compounds within this system, with a size of approximately 875 nm. La is distributed on both sides of the Si element, forming a structure that encapsulates the eutectic Si. Combined with TEM and SAED analysis, it is confirmed that this rare earth phase is the AlSiLa phase with a tetragonal structure. Zhang et al. [33] reported that La preferentially forms AlSiLa or $\text{Al}_2\text{Si}_2\text{La}$ intermetallics within hypoeutectic Al-Si systems. Through thermodynamic calculations of the formation enthalpy of these compounds and the interfacial energy between them and the Al melt,

they determined that La is most likely to form the AlSiLa compound in the Al-Si alloy melt, aligning with our experimental findings.

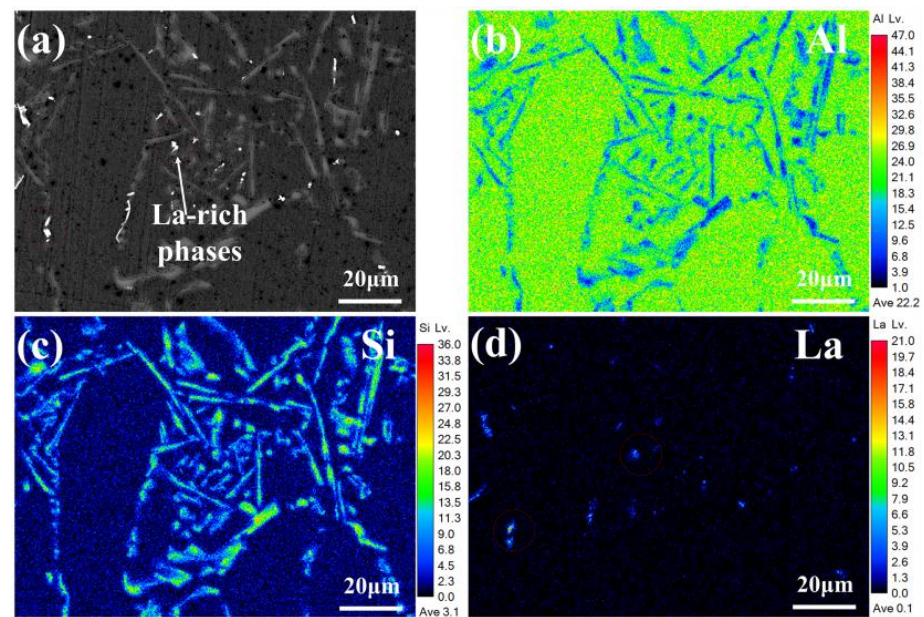


Figure 6. EPMA analysis of La-rich phase particles in Al-7Si-0.06La alloy and EDS elemental maps of (a) BSE image, (b) Al, (c) Si, and (d) La.

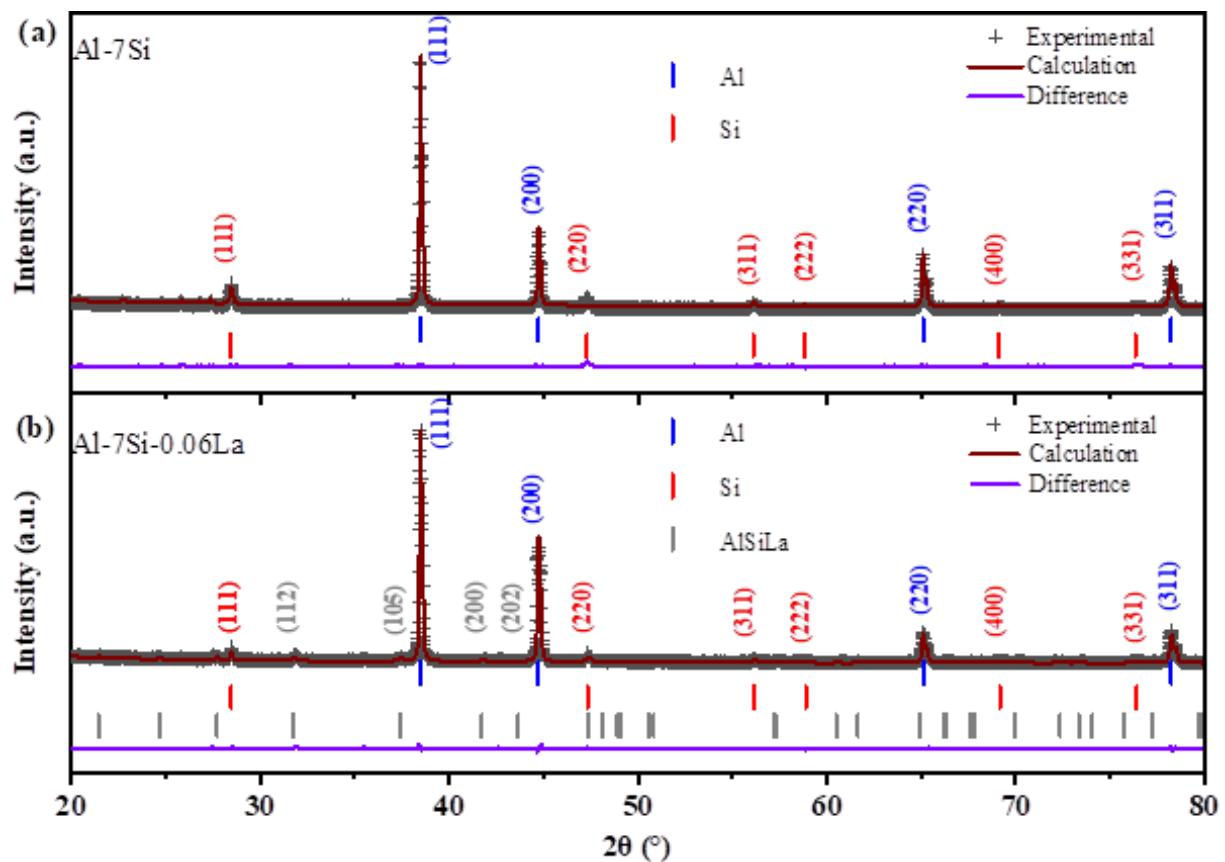


Figure 7. EXRD patterns of (a) Al-7Si alloy and (b) Al-7Si-0.06La alloy.

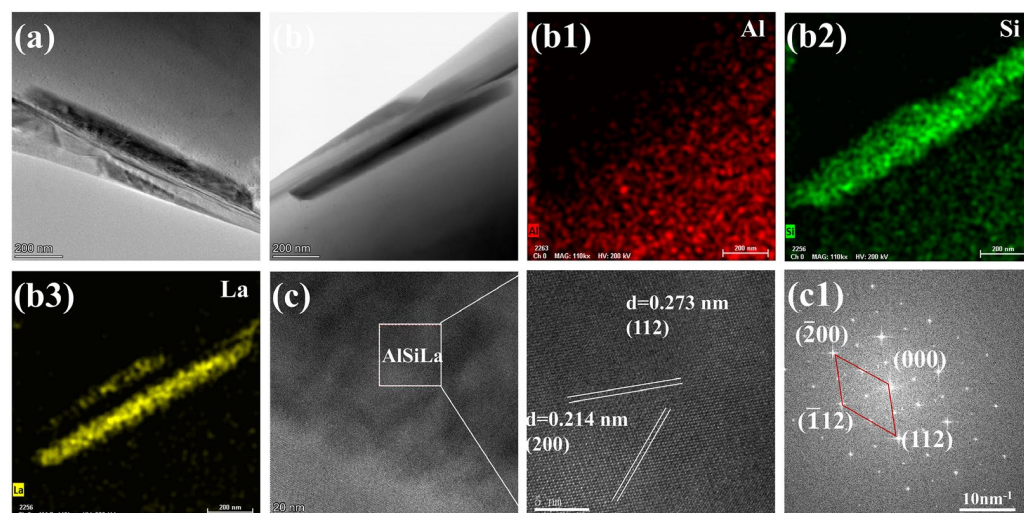


Figure 8. TEM micrographs of eutectic Si particles in Al-7Si-0.06La alloy with corresponding SAED patterns: (a) microstructure of eutectic Si; (b) bright-field of TEM; (b1–b3) EDS; (c) magnification of AlSiLa; (c1) SAED.

3.2. Influence of Trace La Additions on the Solidification Characteristics in Al-7Si Alloy

Figure 9 shows the DSC melting and solidification profiles of Al-7Si alloys containing varying La amounts. The alloy melting process exhibits two distinct endothermic peaks, A and B, corresponding to the Al-Si eutectic reaction and primary α -Al melting, respectively, as shown in Figure 9a. The red dashed line in the figure clearly indicates that the endothermic temperature in the Al-Si eutectic reaction gradually decreases with increasing La content. These findings indicate that La addition effectively suppresses nucleation and development within Al-Si eutectic alloys. Additionally, at lanthanum concentrations of 0.06 wt.% or higher, a new endothermic peak (C) emerges in the DSC curve alongside the development of the eutectic structure of α -Al and Si phases. The intensity of this peak gradually increases with higher La content. This peak arises from AlSiLa phase formation. Furthermore, the coincidence of endothermic peak C with peak (A) of the Al-Si eutectic reaction demonstrates that the AlSiLa phase forms during the Al-Si eutectic reaction stage. The solidification curve in Figure 9b has two exothermic peaks, D and E, corresponding to primary α -Al solidification and the Al-Si eutectic reaction, respectively. During the solidification in hypoeutectic Al-7Si alloy, nucleation commences as the temperature falls below the liquidus. The primary α -Al phase crystallizes first. With further cooling, the amount of α -Al phase gradually increases, while the Al melt correspondingly diminishes. Upon reaching the solidus temperature, the remaining liquid phase undergoes a eutectic reaction, simultaneously forming a eutectic structure made up of α -Al phase and Si phase. In the absence of La, the entire melt solidifies as primary α -Al phases and an eutectic structure containing Si. When the La content added is <0.06%, La can dissolve into the α -Al phase, while the entire liquid phase still transforms into the Al-Si eutectic structure. At La concentrations ≥ 0.06 wt.%, besides the formation of the α -Al phase and Si phase, the rare earth AlSiLa phase also precipitates. This phase grows attached to the eutectic Si, further confirming the growth location of the AlSiLa phase (Figure 8). The formed AlSiLa compounds in the alloy directly impede the movement of free electrons, reducing thermal conductivity. Simultaneously, they act as heterogeneous nucleation sites, refining grains and increasing grain boundaries. This enhances electron scattering, further decreasing thermal conductivity, which explains the decline in thermal conductivity when La content exceeds 0.06%.

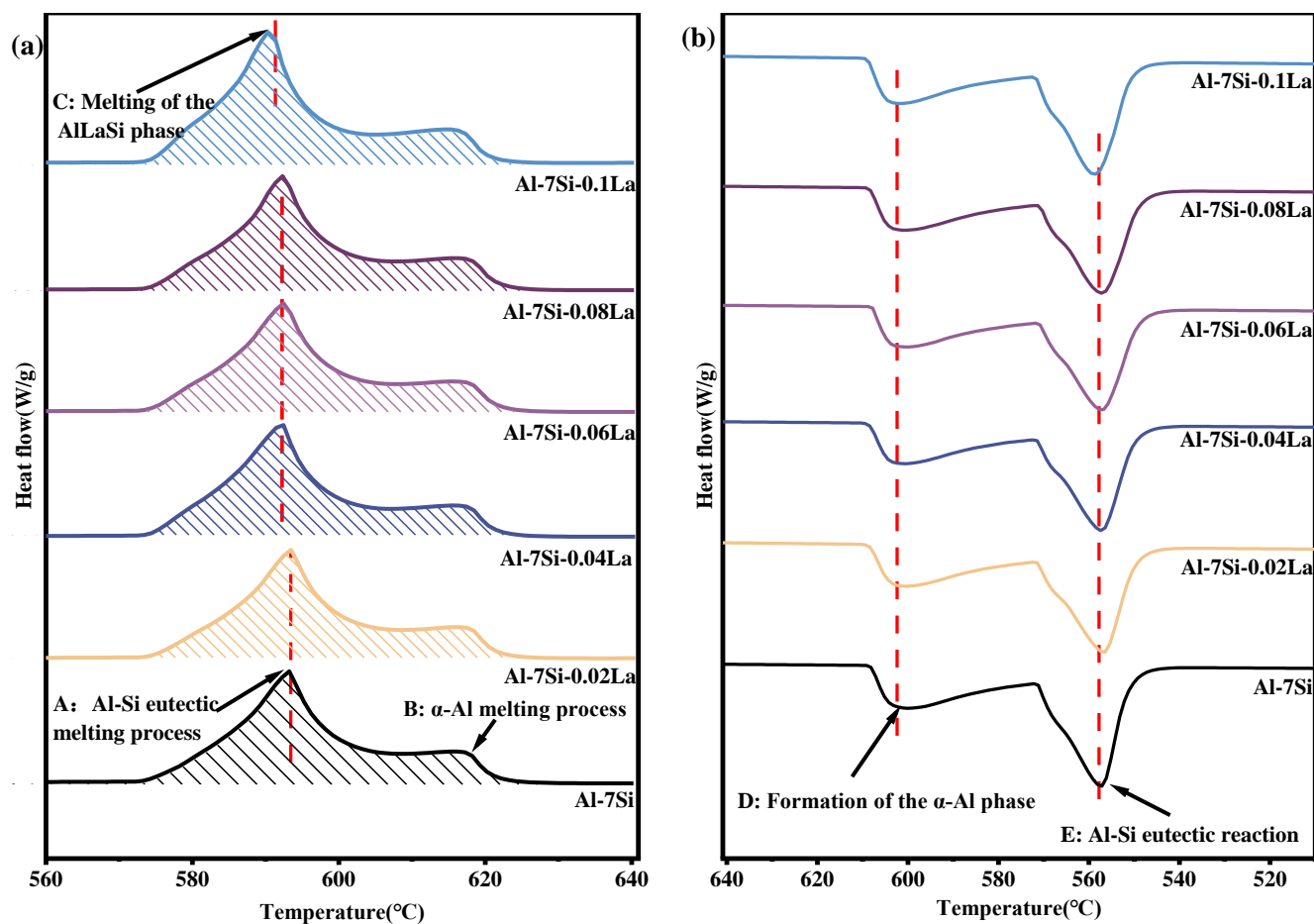


Figure 9. DSC melting and solidification profiles for Al-7Si-XLa alloy: (a) melting curves; (b) solidification curves.

3.3. Influence of Trace La on Thermal Conductivity in Al-7Si Alloy

Table 2 presents density and thermophysical property parameters of the Al-7Si-XLa alloys. Figure 10 shows the influence curve of trace La on the thermal conductivity of the Al-7Si alloy. The base Al-7Si alloy exhibits the lowest thermal conductivity ($155.397 \text{ W} \cdot \text{m}^{-1} \cdot \text{K}^{-1}$). With 0.06 wt.% La addition, the alloy achieves peak thermal conductivity ($179.259 \text{ W} \cdot \text{m}^{-1} \cdot \text{K}^{-1}$), representing a 15.36% gain over the Al-7Si alloy. However, further La additions progressively reduce the thermal conductivity of the Al-7Si alloy. At 0.1 wt.% La, the alloy's thermal conductivity registers $161.645 \text{ W} \cdot \text{m}^{-1} \cdot \text{K}^{-1}$. This value exceeds that of the unmodified alloy by 4.02%.

Table 2. Density and thermophysical properties of Al-7Si-XLa alloys.

	ρ ($\text{g} \cdot \text{cm}^{-3}$)	C_p ($\text{J} \cdot \text{g}^{-1} \cdot \text{K}^{-1}$)	α ($\text{mm}^2 \cdot \text{s}^{-1}$)	κ ($\text{W} \cdot \text{m}^{-1} \cdot \text{K}^{-1}$)	$\Delta\kappa$ ($\text{W} \cdot \text{m}^{-1} \cdot \text{K}^{-1}$)	$\Delta\kappa/\kappa_{\text{unmd}}$ %
Al-7Si	2.651	0.889	65.961	155.397	-	-
Al-7Si-0.02La	2.656	0.968	65.975	169.614	14.217	9.15
Al-7Si-0.04La	2.663	0.941	68.889	172.566	17.169	11.05
Al-7Si-0.06La	2.671	0.957	70.159	179.259	23.862	15.36
Al-7Si-0.08La	2.665	0.825	74.265	163.362	7.965	5.13
Al-7Si-0.1La	2.742	0.839	70.290	161.645	6.248	4.02

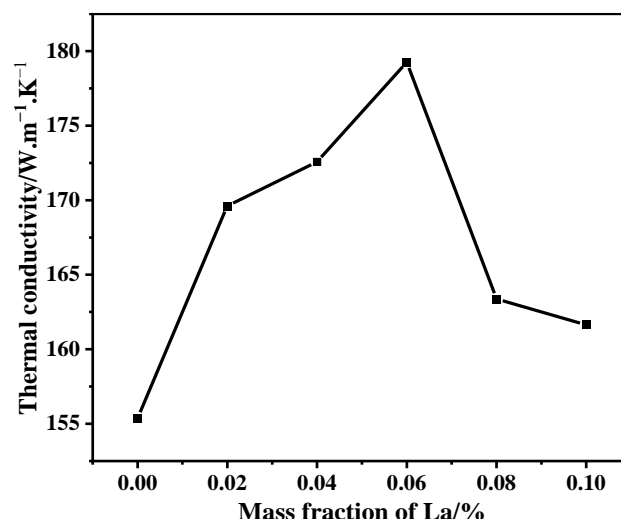


Figure 10. Effect of trace La additions on the thermal conductivity of Al-7Si-XLa alloy.

3.4. Microstructure Development in Al-7Si Alloy Doped with Trace Lanthanum Following 100 Thermal Cycles

The metallographic structure of the Al-7Si-XLa alloy subjected to 100 thermal cycles is presented in Figure 11. Before thermal cycling, eutectic silicon and primary α -Al phase are the main constituents in the Al-7Si alloy. After La modification treatment, eutectic silicon evolved from a plate-like to short rod-like morphology. Following 100 thermal cycles, both primary α -Al and eutectic silicon phases persist, whereas the microstructure undergoes substantial morphological alteration. For the original undeteriorated Al-7Si alloy, the eutectic silicon morphology remained largely unaltered by thermal cycling and still remained plate-like. However, the size increased significantly compared with that before the thermal cycle, and coarsening occurred. Within the Al-7Si alloy with La addition, the morphological variation in eutectic Si is more obvious. Short rod-shaped eutectic Si diminishes, while plate-shaped silicon expands. This indicates that multiple melting–solidification heat cycles cause La burnout, increase plate-like eutectic Si, and weaken the alloy deterioration effect. This phenomenon is attributed to the segregation of La atoms. During thermal cycling, lanthanum atoms migrate along interfaces under thermal activation [34]. At elevated temperatures, La diffuses from grain boundaries into the matrix, reducing its concentration at the interfaces. During cooling, La re-segregates to the grain boundaries. This cyclic migration periodically destabilizes the silicon phase interfaces, promoting repeated dissolution and reprecipitation of silicon particles, and ultimately accelerating their coarsening [34]. Moreover, due to the highly reactive nature of La, oxidation occurs even during thermal cycling in a vacuum tube furnace [35]. This is also a primary reason for grain coarsening.

Figure 12 presents the primary α -Al grain size distribution in Al-7Si-XLa alloy following 100 thermal cycles. Figure 12 reveals that primary crystal α -Al grain size gradually decreases as La content increases after thermal cycling, and this pattern is the same as that before thermal cycling. After the thermal cycling of the original Al-7Si alloy, the primary α -Al grain size was 83.15 μm , which increased by 54 μm compared with that before the thermal cycling. At a La content of 0.06 wt.%, the primary α -Al grain size measured 78.19 μm , which was 5.97% lower than that of the original alloy. With La content increasing to 0.1 wt.%, the alloy's dendrite spacing slightly increased in comparison to the Al-7Si-0.06La alloy, reaching 79.94 μm . This value still represents a 3.86% reduction compared to the original Al-7Si. This demonstrates that optimal La additions effectively suppress

primary α -Al grain coarsening under thermal cycling. However, excessive addition of La will weaken the grain refinement effect.

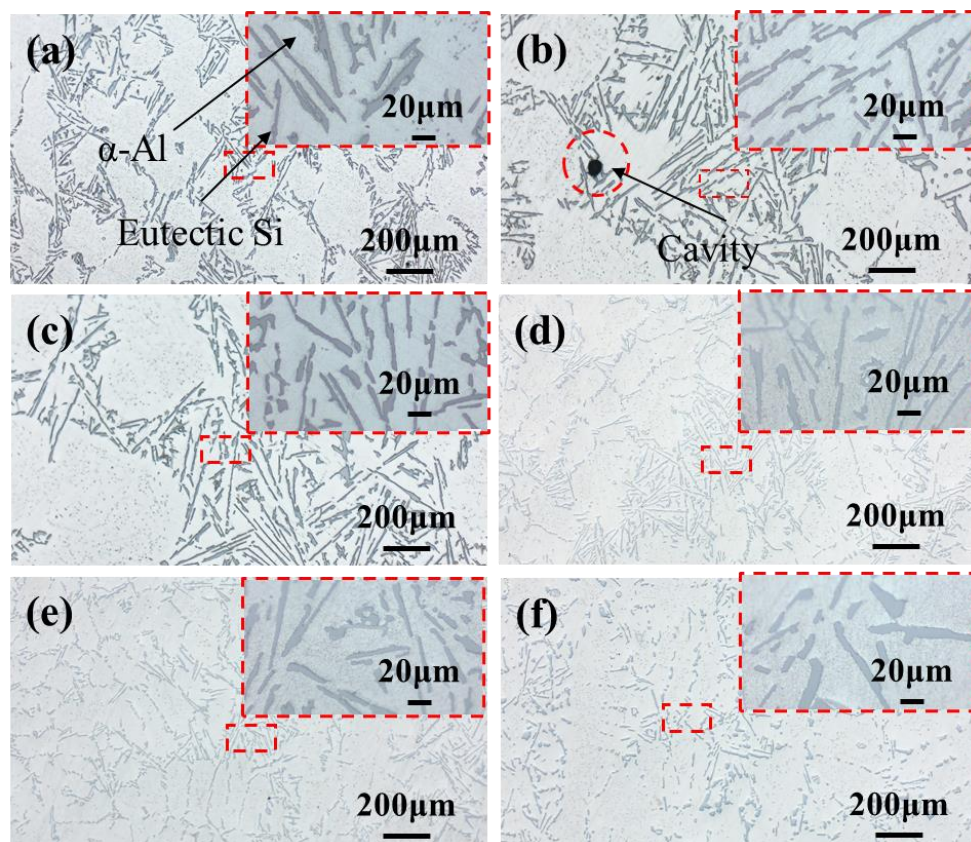


Figure 11. Metallographic microstructure and local magnification of Al-7Si-XLa alloy after 100 thermal cycles: (a) $X = 0$; (b) $X = 0.02$; (c) $X = 0.04$; (d) $X = 0.06$; (e) $X = 0.08$; (f) $X = 0.1$.

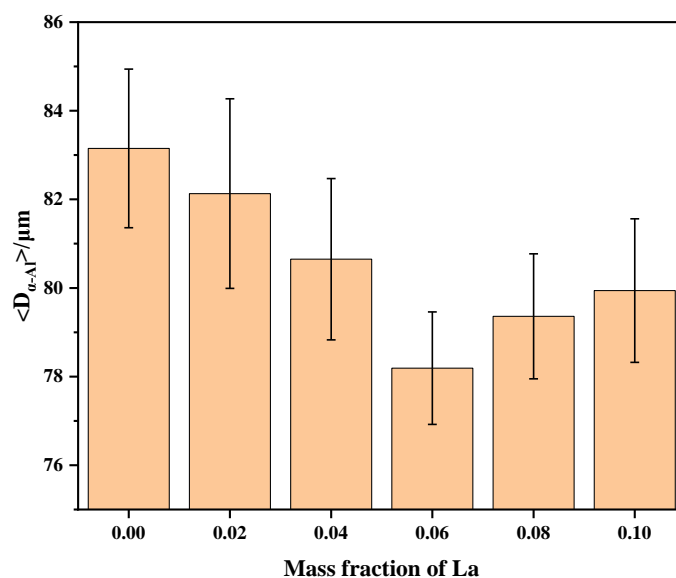


Figure 12. Statistical results of primary α -Al grain size in Al-7Si-XLa alloy after 100 thermal cycles.

3.5. The Effect of Trace La on the Latent Heat of Phase Transformation in Al-7Si Alloy After 100 Thermal Cycles

After 100 thermal cycles, the DSC curves showing the melting and solidification characteristics in the Al-7Si-XLa alloy are presented in Figure 13. Figure 13 indicates that the Al-7Si-XLa alloy retains two clear endothermic and exothermic peaks after 100 thermal

cycles. Furthermore, the DSC peak profiles remain largely unchanged relative to the pre-cycled state. These observations suggest that the alloy's phase composition remains relatively stable throughout thermal cycling. Figure 13a demonstrates that La addition decreases the endothermic peak temperature associated with the Al-Si eutectic reaction. At 0.04 wt.% La, the endothermic temperature of the eutectic of the alloy is the lowest, which is 590.9 °C. Even following 100 thermal cycles, La continues to suppress the nucleation and growth dynamics in the Al-Si eutectic phase during solidification. Analysis of the solidification curve in Figure 13b reveals a slight increase in the eutectic solidification onset temperature for the original Al-7Si alloy, rising from 557.3 °C prior to thermal cycling to 557.9 °C post-cycling. The eutectic reaction solidification temperature of the Al-7Si-0.1La alloy was 556.2 °C, which was 1.7 °C lower than that of the original alloy and 2.6 °C lower than that before the thermal cycle. The eutectic solidification temperature of the alloy is lower than that before the thermal cycle. This phenomenon is mainly because during the thermal cycling process, La in the alloy undergoes burning loss, leading to an increase in the amount of lamellar eutectic Si and a reduction in the alloy's deterioration effect. After multiple thermal cycles, the phase transformation temperature of the alloy remains essentially stable. This is because the phase transformation temperature of the alloy is mainly related to the temperature of its eutectic phase, while the eutectic temperature is only associated with the components of the constituent system and unrelated to the relative content of the components and the phase state. Therefore, after 100 thermal cycles, the alloy's phase transformation temperature shows no significant change.

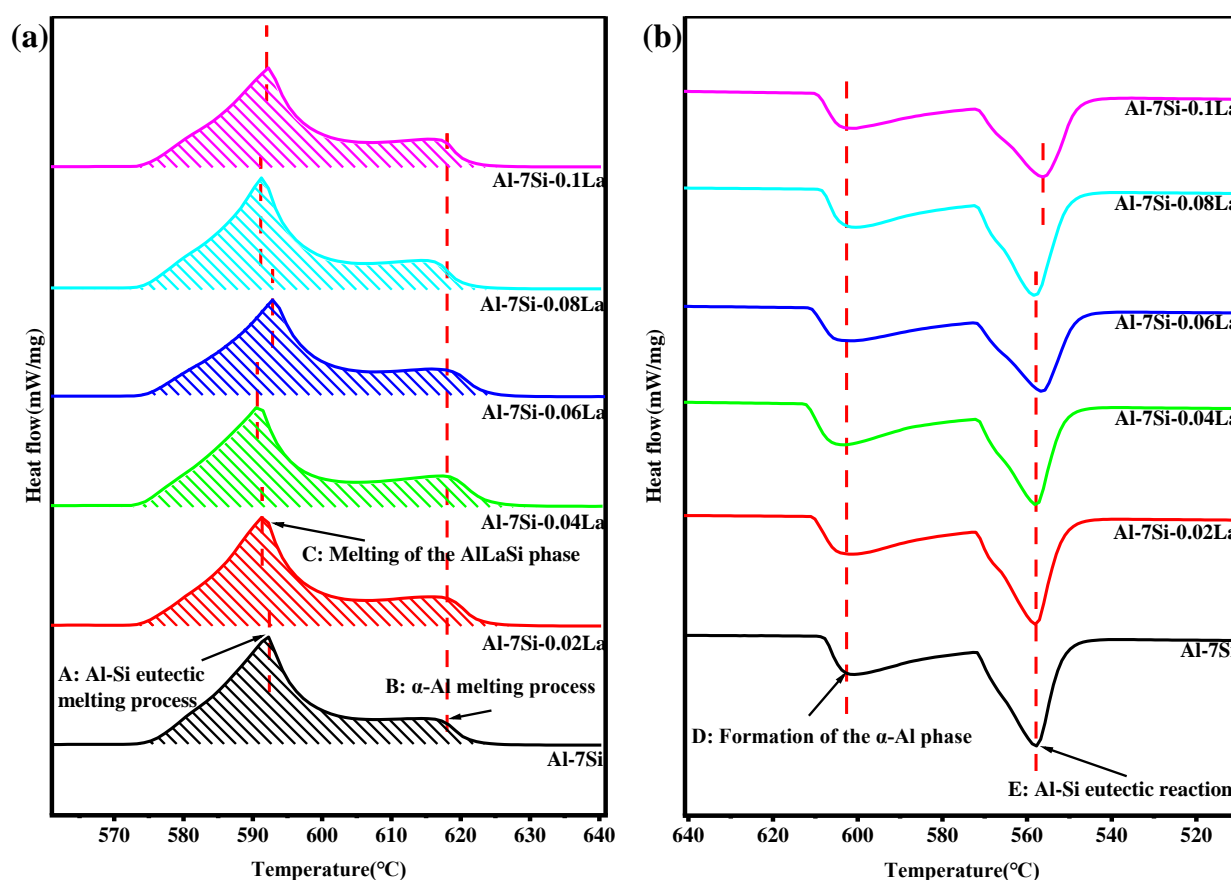


Figure 13. DSC melting and solidification profiles for Al-7Si-XLa alloy following 100 thermal cycles: (a) melting curves; (b) solidification curves.

By integrating the DSC melting curves of the alloy in Figures 9a and 13a, the integral area of the curves (the area of the shaded part in the figure) was calculated, thereby

obtaining the alloy's melting latent heat before and after thermal cycling. Specific data are presented in Table 3. Before thermal cycling, the original Al-7Si alloy had a phase transformation latent heat of 336.9 J/g. As La content increased, the alloy's phase transformation latent heat exhibited a trend of first decreasing and then increasing. When La content reaches 0.02 wt.%, the alloy's phase transformation latent heat drops to the lowest level of 327.8 J/g, 9.1 J/g lower than that of the original alloy. When La content was further increased to 0.1 wt.%, the alloy's phase transformation latent heat gradually rose to 364.9 J/g, with an 8.31% increase compared to the original. After 100 thermal cycles, the alloy's latent heat variation law contrasted with that before thermal cycling, exhibiting a trend of initial increase followed by decrease. The latent heat of phase transformation of the original Al-7Si alloy increased to 342.7 J/g, which was 5.8 J/g higher than that before the thermal cycle. The Al-7Si-0.1La alloy's phase transformation latent heat is the smallest at 328.2 J/g, a 4.23% decrease.

Table 3. DSC measurement results of six Al-7Si-XLa alloy compositions before and after thermal cycling.

Sample	Al-7Si	Al-7Si-0.02La	Al-7Si-0.04La	Al-7Si-0.06La	Al-7Si-0.08La	Al-7Si-0.1La
Latent Heat of Melting (As-Cast) (J/g)	336.9	327.8	330.1	340.4	341.9	364.9
Latent Heat of Melting (Post-Cycling) (J/g)	342.7	353.7	343.7	328.6	338.9	328.2

4. Mechanisms

4.1. The Modification Mechanism of La on Eutectic Si in Al-7Si Alloy

Eutectic Si's modification mechanism primarily involves two approaches. First, from a nucleation standpoint, modifying elements offer heterogeneous nucleation sites that boost eutectic Si's nucleation rate, thereby refining the Si phase [32,36]. Second, modification can be achieved by influencing the crystal growth of Si through two main mechanisms: the Impurity-Induced Twinning (IIT) mechanism along with the Twin-Plane Re-Entrant Edge (TPRE) mechanism [26,30,32,36–39]. The TPRE mechanism holds that eutectic Si forms a sheet-like morphology after multiple growth cycles at the twinning groove. Based on this mechanism, the poisoning of TPRE was proposed. It is believed that the deteriorated atoms aggregate and adsorb at the twinned grooves, restricting eutectic Si growth; it grows isotropically and deteriorates into a fibrous state. The IIT mechanism holds that when the silicon crystal is not deteriorated, the growth rate in the $\langle 112 \rangle$ direction is faster than that in the $\langle 111 \rangle$ direction, and the eutectic Si grows anisotropically into sheets. Crystals impede the uptake of new Si atoms, alter the stacking sequence of Si atoms, and generate numerous twins. Eutectic Si then grows into fibers via the TPRE mechanism. While hypoeutectic Al-Si alloys solidify, as the temperature falls to the eutectic temperature of 577 °C, the Al-Si eutectic reaction takes place. Due to the higher diffusion rate of Si in Al melt relative to Al itself, Si precipitates first to form eutectic Si, while α -Al nucleates and grows on the eutectic Si phase [40]. TSi crystals have a face-centered cubic (FCC) crystal structure. According to the Jackson factor of crystallographic planes [41], the {111} planes preferentially crystallize over the {100} planes when the undercooling is sufficient. Consequently, the external surfaces of eutectic Si are predominantly bounded by {111} planes, as illustrated in Figure 14a. Figure 14b,c show a three-dimensional model of a Si crystal featuring two parallel twin planes (TP1 and TP2). Its outer surface is composed of {111} planes. At the front of the eutectic Si growth interface (red region), twin plane TP1 forms a 141° groove (between planes 2 and 3) and a 219° ridge (between planes 1 and 2) with the external {111} plane [36,42]. As Si atoms continuously deposit within the grooves, nucleation and growth processes occur, transforming planes 1–6 (red region in Figure 14b)

into planes 1*–6* (orange region in Figure 14c). For the unmodified Al-7Si alloy, its twin growth direction runs parallel to the growth direction of eutectic Si, as shown in Figure 4d. This parallel arrangement matches the growth model forecast by the Twin-Plane Re-entrant Edge (TPRE) mechanism [36,43]. However, eutectic Si within the alloy exhibits relatively low twin density on its surface, resulting in limited branching effects from twinning. Furthermore, the preferred growth of eutectic Si along the $\langle 112 \rangle$ direction restricts its ability to alter growth orientation during solidification. These combined factors ultimately determine the plate-like distribution of eutectic Si inside the α -Al matrix [44–46].

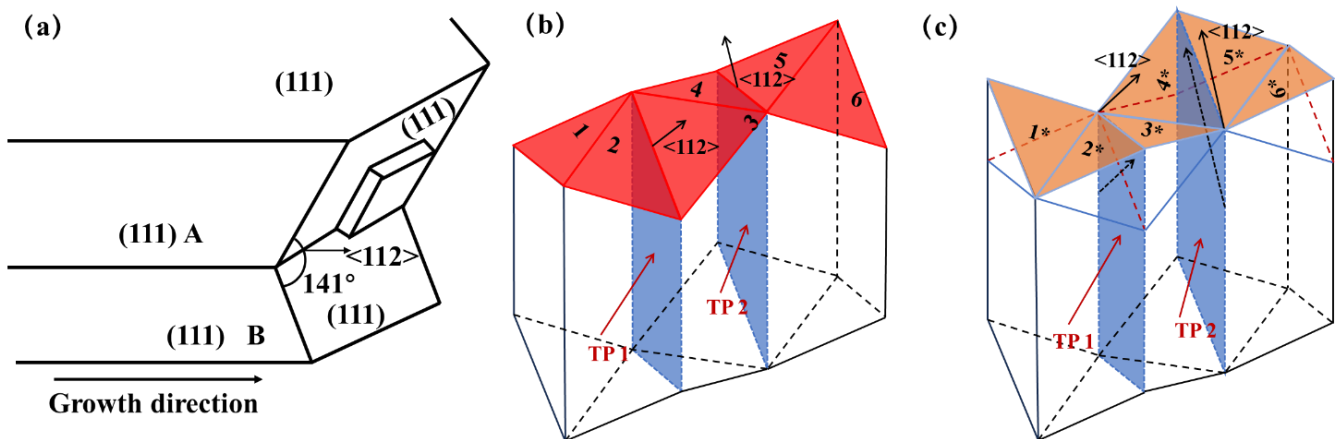


Figure 14. Twin-Plane Re-entrant Edge (TPRE) growth mechanism. (a) Growth Mechanism of Twin Grooves on the (111) Plane of Eutectic Silicon; (b) 3D Model of Eutectic Silicon Crystal with Two Parallel Twin Planes (TP1 and TP2): Two grooves with an angle of 141° are formed between the 2nd plane & the 3rd plane, and between the 4th plane & the 5th plane; (c) Silicon atoms stack and grow in an alternating cycle within the twin grooves, Two convex ridges with an angle of 219° are formed between the 2nd plane & the 3rd plane, and between the 4th plane & the 5th plane, the eutectic silicon grows along the $\langle 112 \rangle$ direction.

Lu et al. [47] computationally demonstrated that the primary condition for modifying elements to induce high-density twinning on eutectic Si surfaces is a modifying element-to-Si atomic radius ratio of approximately 1.646. The radius ratio between La (0.187 nm) and Si (0.118 nm) is 1.59, which closely approaches this critical value. Consequently, during Al-7Si alloy solidification, La atoms can adsorb on the eutectic Si's growth front. Furthermore, as seen in Figure 4d, misorientation steps exist at interfaces between α -Al and eutectic Si. These step sites offer favorable positions for La adsorption, in full agreement with the Twin-Plane Re-entrant Edge (TPRE) mechanism. Figure 15 schematically illustrates La atoms adhered at the Si's growth front, inducing high-density twinning. When twins A and B grow horizontally in the direction of eutectic Si growth, La adsorption at the growth front alters the stacking order of {111}Si planes. This induces the nucleation of new twins B and C on the surface of twin A, which subsequently grow along new $\langle 112 \rangle$ Si directions, forming angles of either 70.5° or 109.5° with the original growth direction [29]. Adding La reduces the size of eutectic Si and alters its morphology from anisotropic plate-like to isotropic short rod-like structures [48–53]. Furthermore, La introduction induces the formation of high-density twins with characteristic 70.5° angles on the surface of eutectic Si particles [48,51,52], as shown in Figure 5.

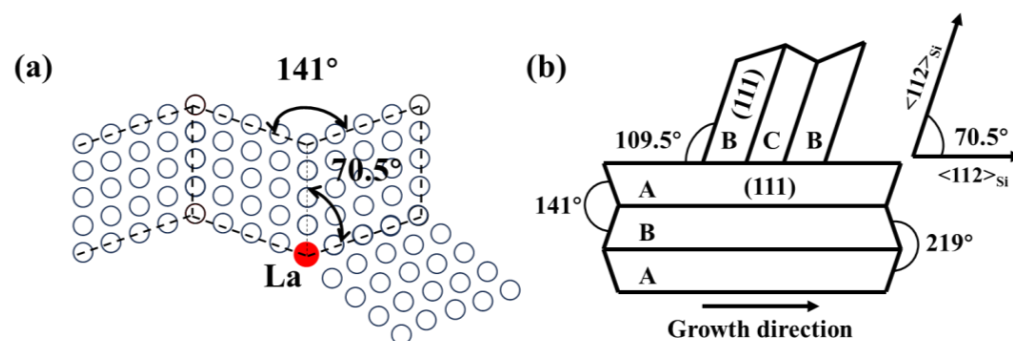


Figure 15. (a) Schematic illustration of La atoms embedded in eutectic [111]Si planes inducing high-density twinning within the Si crystal; (b) growth and branching mechanism model of eutectic Si with 70.5° angular relationships.

4.2. Influence of La on the Thermal Conduction Mechanism of Eutectic Si in Al-7Si Alloys

Heat conduction in metals consists of two parts: free electron conduction and phonon conduction [53]. However, at room temperature, free electrons carry over 90% of the total heat in metallic materials [14]. Based on the Wiedemann–Franz law, the thermal conductivity for free electrons is calculated as presented in Formula (2) [11].

$$K_e = L_0 \sigma T \quad (2)$$

where K_e denotes the thermal conductivity of electrons, L_0 is the Lorenz number, σ is the electrical conductivity, and T is the absolute temperature.

Based on the classical electron theory, electrical conductivity (σ) and resistivity (ρ) are reciprocal physical quantities that characterize a material's electrical properties. Therefore, the thermal conductivity of free electrons can be expressed using Formula (3).

$$K_e = \frac{L_0 T}{\rho} \quad (3)$$

According to Bloch's theory, free electrons encounter no resistance when moving through a perfect periodic potential field of an ideal metal crystal, resulting in theoretically zero resistivity [54]. However, actual crystal structures contain defects such as lattice distortions, dislocations, and impurity atoms. These defects act as scattering centers that impede electron motion and reduce their mean free path [55]. This is the primary mechanism of electrical resistance. In Al-Si alloys, the continuously distributed α -Al phase provides a high concentration of free electrons through metallic bonding and, due to its low electrical resistivity ($2.83 \times 10^{-8} \Omega \cdot \text{m}$), constitutes the primary pathway for electrical and thermal conduction. In contrast, the eutectic Si phase ($2.14 \times 10^3 \Omega \cdot \text{m}$) exhibits extremely low solid solubility (only 0.05% at room temperature) and predominantly precipitates in plate-like or blocky forms at grain boundaries or within grains of the α -Al matrix. These Si particles severely disrupt the aluminum matrix, obstruct the movement of free electrons, enhance electron scattering, and consequently reduce both the thermal and electrical conductivity of the alloy. Research shows that reducing the size of Si phases significantly weakens interface scattering effects, thereby enhancing the alloy's thermal conductivity [56,57]. This mechanism is well explained by the Wiedemann–Franz law (Formula (1)): since electron thermal conductivity (K) in metals is inversely proportional to electrical resistivity (ρ), reduced electron scattering simultaneously improves both electrical and thermal performance [11]. Thus, controlling the morphology of eutectic Si phases represents an effective approach to enhance the thermal conductivity of Al-Si alloys.

Comparison of La-modified and unmodified Al-7Si alloys reveals that La modification significantly enhances thermal conductivity by altering the morphology and size of eutectic Si. In the unmodified alloy (Figure 1a), coarse plate-like eutectic Si phases are randomly distributed and interconnected, severely fragmenting the α -Al matrix. This plate-like morphology dramatically increases electron scattering probability, impeding free electron movement through the alloy. Consequently, the thermal conductivity measures $155.40 \text{ W}\cdot\text{m}^{-1}\cdot\text{K}^{-1}$. During La modification, La atoms selectively adsorb onto eutectic Si growth interfaces, inducing high-density twinning within the silicon phase (Figure 5c). This forces the eutectic silicon to transition from anisotropic to near-isotropic growth, ultimately forming short rod-like and fibrous structures as shown in Figure 1c. After modification, fine rod-shaped eutectic Si disperses uniformly, significantly enhancing connectivity within the α -Al matrix while reducing electron scattering at phase interfaces and pores. Consequently, electron transport efficiency improves. Compared to coarse plate-like structures, this refined morphology substantially decreases interface scattering and reduces tortuosity in electron transport paths, thereby effectively increasing electron mobility (μ_e) [58,59]. Electron scattering within the Al-7Si alloy is shown in Figure 16. Additionally, the modification treatment refines the primary α -Al grains, shortening the travel distance for electrons crossing grain boundaries. The optimized eutectic Si morphology—characterized by reduced size and uniform distribution—synergistically enhances electron transport efficiency [60]. Furthermore, the reactive nature of rare-earth La facilitates chemical reactions with impurity elements (such as H and Fe) during melting, along with effective adsorption of these impurities. This significantly reduces impurity content. The diminished impurities mitigate lattice distortion, thereby decreasing scattering of free electrons. These synergistic mechanisms collectively enhance the alloy's thermal conductivity.

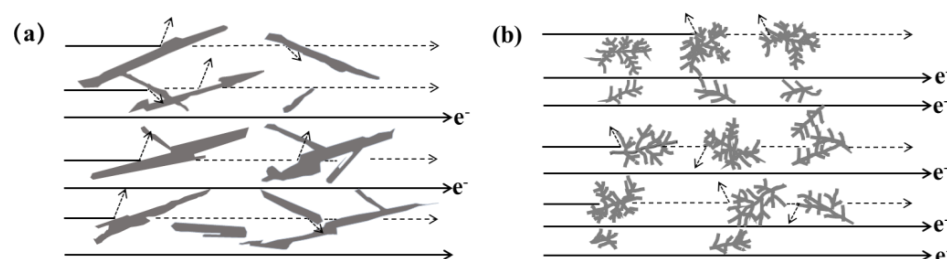


Figure 16. Schematic illustration of electron collisions with differently shaped eutectic Si in Al-Si alloys: (a) plate-like structures; (b) short rod-like structures.

However, excessive La addition promotes precipitation of AlSiLa intermetallic compounds at grain boundaries. These compounds not only directly obstruct free electron movement but also increase interface density and complexity (including phase/grain boundaries), thereby elevating electron scattering probability. Consequently, the alloy's thermal conductivity decreases markedly [60].

5. Conclusions

In this study, a hypoeutectic Al-7Si phase change heat storage alloy with trace La was fabricated via smelting and casting. Systematic study was conducted on the effect of trace La on its microstructure and heat storage performance, yielding the following conclusions:

- (1) Adding La transformed eutectic Si particles from plate-like to short rod-like structures, with a marked reduction in size; the modification effect was optimal at 0.06 wt.% La. Meanwhile, primary α -Al's grain size gradually decreased as La content increased. At 0.06 wt.% La, it decreased by 35.33% compared with the original alloy. Trace amounts of La can induce the generation of high-density interlaced twins on eutectic Si surface, with the twin plane being the $\{111\}$ Si plane and the twin direction being $\langle 111 \rangle$ Si. In

addition, La will also form the AlSiLa phase in the alloy, which is distributed near the eutectic Si and wraps around the eutectic Si.

- (2) Adding La can significantly enhance the thermal conductivity of the Al-7Si alloy. At a La content of 0.06 wt.%, the alloy's thermal conductivity peaked at $179.259 \text{ W}\cdot\text{m}^{-1}\cdot\text{K}^{-1}$, 15.36% higher than the original alloy. Excess La ($\geq 0.06 \text{ wt.}\%$) promotes the formation of AlSiLa intermetallic compounds, impedes free electron movement, and diminishes thermal conductivity.
- (3) Adding La can significantly improve the alloy's high-temperature oxidation resistance. After oxidizing the original Al-7Si alloy at a constant 700°C for 96 h, its oxidation weight gain per unit of area amounted to $3.908 \times 10^{-3} \text{ g}\cdot\text{cm}^{-2}$. When 0.1 wt.% La was added, the oxidative gain per unit area decreased to $1.931 \times 10^{-3} \text{ g}\cdot\text{cm}^{-2}$, a reduction of 50.59%. The alloy's oxidation rate gradually slows as oxidation time increases.
- (4) After 100 thermal cycles, the phase transition temperature in the alloy stays largely unaltered. However, the metamorphic effect of La diminishes, the quantity of plate-like eutectic Si increases, and when the La content is $\geq 0.06 \text{ wt.}\%$, the latent heat of phase transition decreases compared with that before thermal cycling. Among them, the latent heat of phase transition of the original Al-7Si alloy increases from 336.9 J/g to 342.7 J/g ; the latent heat of phase transition of the Al-7Si-0.06La alloy decreases from 340.4 J/g to 328.6 J/g ; and the latent heat of phase transition of the Al-7Si-0.1La alloy decreases from 364.9 J/g to 328.2 J/g . La can effectively restrain the growth of primary α -Al grains during thermal cycles. At a La content of 0.06 wt.%, the size of primary α -Al grains was $78.19 \mu\text{m}$, 5.97% smaller than that of the original alloy. As La content increased to 0.1 wt.%, the alloy's dendrite spacing was $79.94 \mu\text{m}$, 3.86% smaller than the original Al-7Si alloy.

Author Contributions: Conceptualization, J.-Y.Y.; methodology, J.-C.L., Y.S. and R.-Y.Z.; validation, Y.S. and R.-Y.Z.; formal analysis, J.-C.L., Y.S. and R.-Y.Z.; investigation, J.-C.L. and L.W.; data curation, J.-Y.Y.; writing—original draft preparation, J.-Y.Y.; writing—review and editing, R.-Y.Z.; visualization, L.W.; supervision, Y.S. and R.-Y.Z. All authors have read and agreed to the published version of the manuscript.

Funding: This research received no external funding.

Data Availability Statement: The original contributions presented in this study are included in the article. Further inquiries can be directed to the corresponding authors.

Conflicts of Interest: Author Yi Sui was employed by the company Hangzhou Baogang Rare Earth Technology Development Co., Ltd. The remaining authors declare that the research was conducted in the absence of any commercial or financial relationships that could be construed as a potential conflict of interest.

References

1. Jiang, Z.; Zou, B.Y.; Cong, L.; Xie, C.P.; Li, C.; Jiao, G.; Zhao, Y.Q.; Nei, B.J.; Zhang, T.T.; Ge, Z.W.; et al. Recent progress and outlook of thermal energy storage technologies. *Energy Storage Sci. Technol.* **2022**, *11*, 2746–2771.
2. Liu, W.; Li, Z.M.; Liu, M.Y.; Yang, C.Y.; Mei, C.; Li, Y. Review of high-temperature phase change heat storage material preparation and applications. *Energy Storage Sci. Technol.* **2023**, *12*, 398–430.
3. Feng, Y.F.; Jiang, S.J.; Fu, X.; Chen, Y. Current status of heat storage technology and research progress of phase change thermal storage materials. *Inf. Rec. Mater.* **2023**, *24*, 32–36.
4. Xiao, J.B.; Zou, B.; Zhuang, Y.J.; Liu, C.Z.; Li, C.C.; Chen, J. Research and application on thermal conduction performance of metal foam composite phase change system. *J. Cent. South Univ. (Sci. Technol.)* **2022**, *53*, 4687–4699.
5. Abd El-Hamid, M.; Wei, G. Effect of varying the thermophysical properties of phase change material on the performance of photovoltaic/thermal-PCM hybrid module numerically. *J. Energy Storage* **2024**, *86*, 111326. [[CrossRef](#)]
6. Sadiq, H.H.; Mussa, M.A. Numerical study of thermal conductivity effect on the performance of thermal energy storage. *J. Eng.* **2022**, *28*, 57–77. [[CrossRef](#)]

7. Bie, Y.; Li, M.; Malekian, R.; Chen, F.; Feng, Z.K.; Li, Z.X. Effect of phase transition temperature and thermal conductivity on the performance of Latent Heat Storage System. *Appl. Therm. Eng.* **2018**, *135*, 218–227. [\[CrossRef\]](#)
8. Deng, T.X.; Luan, D.C.; Hu, Z.H.; Hu, Z.H.; Ren, Y.; Zuo, C.M.; Li, Y.; Zhuo, X.Y.; Wang, Z.Y. Research Progress of Aluminum Based Phase Change Metal Materials for Thermal Energy Storage. *Mater. China* **2022**, *41*, 653–660.
9. Chen, Z.G.; Zhao, J.W.; Chen, X.S.; Dai, G.Z.; Han, J. High Temperature Oxidation Resistance of Al-Cu-Si Based Alloy Heat Storage Material. *Hot Work. Technol.* **2021**, *50*, 76–79.
10. Zhao, Y.; Liu, H.; Zhao, C. Experimental study on the cycling stability and corrosive property of Al-Si alloys as phase change materials in high-temperature heat storage. *Sol. Energy Mater. Sol. Cells* **2019**, *203*, 110165. [\[CrossRef\]](#)
11. Powell, R. Correlation of metallic thermal and electrical conductivities for both solid and liquid phases. *Int. J. Heat Mass Transf.* **1965**, *8*, 1033–1045. [\[CrossRef\]](#)
12. Lu, L.; Nogita, K.; Dahle, A. Combining Sr and Na additions in hypoeutectic Al-Si foundry alloys. *Mater. Sci. Eng. A* **2005**, *399*, 244–253. [\[CrossRef\]](#)
13. Cui, X.L.; Cui, H.W.; Wu, Y.Y.; Liu, X.F. The improvement of electrical conductivity of hypoeutectic Al-Si alloys achieved by composite melt treatment. *J. Alloys Compd.* **2019**, *788*, 1322–1328. [\[CrossRef\]](#)
14. Gan, J.Q.; Huang, Y.J.; Wen, C.; Du, J. Effect of Sr modification on microstructure and thermal conductivity of hypoeutectic Al-Si alloys. *Trans. Nonferrous Met. Soc. China* **2020**, *30*, 2879–2890. [\[CrossRef\]](#)
15. Liu, D.Y.; Yu, X.Y.; Gao, W.L.; Mao, G.L.; Gao, Y.L. Role of Sb Element in Casting Al-Si Alloy. *Hot Work. Technol.* **2022**, *51*, 1–5+12.
16. Elgallad, E.M.; Ibrahim, M.F.; Doty, H.W.; Samuel, F.H. Microstructural characterisation of Al-Si cast alloys containing rare earth additions. *Philos. Mag.* **2018**, *98*, 1337–1359. [\[CrossRef\]](#)
17. Jiang, W.M.; Fan, Z.T.; Dai, Y.C.; Chi, L. Effects of rare earth elements addition on microstructures, tensile properties and fractography of A357 alloy. *Mater. Sci. Eng. A* **2014**, *597*, 237–244. [\[CrossRef\]](#)
18. Li, Q.L.; Xia, T.D.; Lan, Y.F.; Zhao, W.J.; Fan, L.; Li, P.F. Effect of rare earth cerium addition on the microstructure and tensile properties of hypereutectic Al–20% Si alloy. *J. Alloys Compd.* **2013**, *562*, 25–32. [\[CrossRef\]](#)
19. Mao, G.L.; Liu, S.G.; Wu, Z.; Zhu, C.C.; Gao, W.L. The effects of Y on primary α -Al and precipitation of hypoeutectic Al-Si alloy. *Mater. Lett.* **2020**, *271*, 127795. [\[CrossRef\]](#)
20. Mao, F.; Wei, S.Z.; Ou, L.Y.; Zhang, C.; Wang, X.D.; Cao, Z.Q. Different influences of rare earth Eu addition on primary Si refinement in hypereutectic Al-Si alloys with varied purity. *Materials* **2019**, *12*, 3505. [\[CrossRef\]](#)
21. Bhatt, B.; Martucci, A.; Virgillito, E.; Gobber, F.; Bondioli, F.; Manfredi, D.; Lombardi, M.; Fino, P. Deciphering Microstructures and Phases of Gas-Atomised Novel Al-Fe-Si-Cr-Ni Alloys. *Metals* **2024**, *14*, 17. [\[CrossRef\]](#)
22. Li, Y.; Wang, S.R.; Xiao, Z.; Mingyang Du, M.Y.; Zhang, Z.; Liu, M.J.; Li, P.N. The effect of Si content on the microstructure and thermal conductivity of Al-XSi-3Cu-5Mg alloys produced by laser additive manufacturing. *J. Alloys Compd.* **2025**, *1034*, 181341. [\[CrossRef\]](#)
23. Jeyaprakash, N.; Moinuddin, S.Q.; Alnamasi, K.; Alsharif, A. Effect of post-heat treatment cooling strategies on Si morphology and nano-mechanical behavior of additively manufactured AlSi10Mg alloy. *J. Mater. Res. Technol.* **2025**, *36*, 8308–8324. [\[CrossRef\]](#)
24. Zhou, X.Y.; Chao, P.; Luke, S.; Lien, H.H.; Hunter, A.H.; Misra, A.; Shahani, A.J. Three-dimensional morphology of an ultrafine Al-Si eutectic produced via laser rapid solidification. *Scr. Mater.* **2023**, *232*, 115471. [\[CrossRef\]](#)
25. Zhu, W.Q.; Yu, M.Z.; Tang, X.; Chen, X.Y.; Xu, Z.B.; Zeng, J.M. Effect of Er and Si on Thermal Conductivity and Latent Heat of Phase Transformation of Aluminum-Based Alloy. *Acta Metall. Sin.* **2020**, *56*, 1485–1494.
26. Chen, Z.Q.; Jia, J.Y.; Hu, W.X.; Wang, W.; Wang, X.Q. Combining effect of Er and Sr on microstructure and mechanical properties of as-casted A356 alloy. *Rare Met. Mater. Eng.* **2020**, *49*, 3388–3394.
27. Zheng, Q.; Zhang, L.; Jiang, H.; Zhao, J.Z.; He, J. Effect mechanisms of micro-alloying element La on microstructure and mechanical properties of hypoeutectic Al-Si alloys. *J. Mater. Sci. Technol.* **2020**, *47*, 142–151. [\[CrossRef\]](#)
28. Lu, M.; Ye, Z.F.; Zheng, Q.J.; Jiang, H.X.; Zhao, J.Z.; He, J.; Zhang, L.L. Effects of Micro-alloying Element La on Microstructures and Properties of Al-0.6Mg-0.6Si Alloy. *Spec. Cast. Nonferrous Alloys* **2021**, *41*, 1494–1499.
29. Pourbahari, B.; Emamy, M. Effects of La intermetallics on the structure and tensile properties of thin section gravity die-cast A357 Al alloy. *Mater. Des.* **2016**, *94*, 111–120. [\[CrossRef\]](#)
30. Wu, X.Y.; Zhang, H.R.; Jiang, H.T.; Mi, Z.L.; Zhang, H. Multi-refinement effect of rare earth lanthanum on α -Al and eutectic Si phase in hypoeutectic Al-7Si alloy. *Metals* **2020**, *10*, 621. [\[CrossRef\]](#)
31. GB/T 43589-2023; Gold Alloys for Adornment—Determination of Multi-Element Contents by Laser Ablation-Inductively Coupled Plasma Mass Spectrometry. China Standards Press: Beijing, China, 2023.
32. Li, J.H.; Albu, M.; Hofer, F.; Schumacher, P. Solute adsorption and entrapment during eutectic Si growth in Al-Si-based alloys. *Acta Mater.* **2015**, *83*, 187–202. [\[CrossRef\]](#)
33. Zhang, L.L.; Ji, Z.W.; Zhao, J.Z.; He, J.; Jiang, H.X. Key Factors influencing eutectic Si modification in Al-Si hypoeutectic alloy by trace La. *Acta Metall. Sin.* **2023**, *59*, 1541–1546.
34. Li, Y.X.; Liu, J.Y.; Zhang, J.C.; Li, H.F. Microstructure evolution of hypereutectic Al-Si alloy with high Si content during semi-solid remelting. *Chin. J. Nonferrous Met.* **2014**, *24*, 2287–2294. [\[CrossRef\]](#)

35. Du, C.; Jin, S.; Fang, Y.; Li, J.; Hu, S.Y.; Yang, T.T.; Zhang, Y.; Huang, J.Y.; Sha, G.; Wang, Y.G.; et al. Ultrastrong nanocrystalline steel with exceptional thermal stability and radiation tolerance. *Nat. Commun.* **2018**, *9*, 5389. [\[CrossRef\]](#)
36. Liu, X.R.; Zhang, Y.D.; Beausir, B.; Liu, F.; Esling, C.; Yu, F.X.; Zhao, X.; Zuo, L. Twin-controlled growth of eutectic Si in unmodified and Sr-modified Al-12.7%Si alloys investigated by SEM/EBSD. *Acta Mater.* **2015**, *97*, 338–347. [\[CrossRef\]](#)
37. Li, J.H.; Wang, X.D.; Ludwig, T.H.; Tsunekawa, Y.; Arnberg, L.; Jiang, J.Z.; Schumacher, P. Modification of eutectic Si in Al-Si alloys with Eu addition. *Acta Mater.* **2015**, *84*, 153–163. [\[CrossRef\]](#)
38. Chen, J.; Wen, F.; Liu, C.; Li, W.; Zhou, Q.; Zhu, W.; Zhang, Y.; Guan, R. The microstructure and property of Al-Si alloy improved by the Sc-microalloying and Y₂O₃ nano-particles. *Sci. Technol. Adv. Mater.* **2021**, *22*, 205–217. [\[CrossRef\]](#) [\[PubMed\]](#)
39. Zhou, P.F.; Gu, W.L.; Lu, C.X.; Yang, S.G.; Sun, Y. Interfacial Stability and Branch Growth of Eutectic Si Under Different Solidification Conditions. *Foundry* **2022**, *71*, 1095–1100.
40. Nafisi, S.; Ghomashchi, R.; Vali, H. Eutectic nucleation in hypoeutectic Al-Si alloys. *Mater. Charact.* **2008**, *59*, 1466–1473. [\[CrossRef\]](#)
41. He, Y.; Zhang, H.L.; Li, T.; Wang, X.T. Calculation of Jackson's factor of Mg₂Si in Mg melt using coordination polyhedron. *J. Alloys Compd.* **2013**, *581*, 494–497. [\[CrossRef\]](#)
42. Pineau, A.; Guillemot, G.; Reinhart, G.; Nguyen, T.H.; Dabo, Y.; Mangelinck, N.N. Three-dimensional cellular automaton modeling of silicon crystallization with grains in twin relationships. *Acta Mater.* **2020**, *191*, 230–244. [\[CrossRef\]](#)
43. Xu, Y.; Deng, Y.; Casari, D.; Li, Y.; Zhao, D.; Niu, X. In-situ X-radiographic study of nucleation and growth behaviour of primary silicon particles during solidification of a hypereutectic Al-Si alloy. *J. Alloys Compd.* **2020**, *832*, 154948. [\[CrossRef\]](#)
44. Li, J.; Barrirero, J.; Engstler, M.; Hötzel, R.; Garcia, P.; Renner, M.; Schmidt, M.; Weygand, D.; Wagner, J.; Hahn, H. Nucleation and Growth of Eutectic Si in Al-Si Alloys with Na Addition. *Metall. Mater. Trans. A* **2015**, *46*, 1300–1311. [\[CrossRef\]](#)
45. Li, Q.; Zhao, S.; Li, B.; Rong, Y.; Zhang, L. Modification of multi-component Al-Si casting piston alloys by addition of rare earth yttrium. *Mater. Res. Express* **2019**, *6*, 106525. [\[CrossRef\]](#)
46. Mao, F.; Qiao, Y.F.; Zhang, P.; Ou, L.M.; Chen, C.; Zhang, C.; Wang, Y. Modification Mechanism of Rare Earth Eu on Eutectic Si in Hypoeutectic Al-Si Alloy. *Int. J. Met.* **2021**, *16*, 634–645. [\[CrossRef\]](#)
47. Lu, S.; Hellawell, A. The mechanism of silicon modification in aluminum-silicon alloys: Impurity induced twinning. *Metall. Trans. A* **1987**, *18*, 1721–1733. [\[CrossRef\]](#)
48. Mao, F.; Wei, S.; Chong, C.; Zhang, C.; Wang, X.D.; Cao, Z.Q. Modification of the silicon phase and mechanical properties in Al-40Zn-6Si alloy with Eu addition. *Mater. Des.* **2020**, *186*, 108268. [\[CrossRef\]](#)
49. Mao, G.L.; Yan, H.; Zhu, C.C.; Zhen, W.; Gao, W.L. The varied mechanisms of yttrium (Y) modifying a hypoeutectic Al-Si alloy under conditions of different cooling rates. *J. Alloys Compd.* **2019**, *806*, 909–916. [\[CrossRef\]](#)
50. Li, L.F.; Li, D.Q.; Luo, M.; Zhang, Y.Z.; Kang, Y.T.; Zhu, Q.; Midson, S.P. Influence of Rare Earth Additions on the Microstructure and Mechanical Properties of Al7Si0.3Mg Alloys Processed by Semi-Solid Die Casting and Gravity Die Casting. *Solid State Phenom.* **2019**, *285*, 69–74. [\[CrossRef\]](#)
51. De Giovanni, M.; Kaduk, J.; Srirangam, P. Modification of Al-Si Alloys by Ce or Ce with Sr. *JOM* **2018**, *71*, 426–434. [\[CrossRef\]](#)
52. Liu, Q.; Liu, M.W.; Xu, C.; Xiao, W.L.; Yamagata, H.; Xie, S.H.; Ma, C.L. Effects of Sr, Ce and P on the microstructure and mechanical properties of rapidly solidified Al 7Si alloys. *Mater. Charact.* **2018**, *140*, 290–298. [\[CrossRef\]](#)
53. Madelung, O.; White, G.K. Thermal Conductivity of Pure Metals and Alloys. In *Landolt-Börnstein—Group III Condensed Matter*; Springer: Berlin/Heidelberg, Germany, 1991; Volume 15c. [\[CrossRef\]](#)
54. Takeuchi, H. Quantum Elliptic Vortex in a Nematic-Spin Bose-Einstein Condensate. *Phys. Rev. Lett.* **2021**, *12*, 126. [\[CrossRef\]](#)
55. Vandersluis, E.; Emadi, P.; Andilab, B.; Gruzleski, J.; Chen, X.G. The role of silicon morphology in the electrical conductivity and mechanical properties of as-cast B319 aluminum alloy. *Metall. Mater. Trans. A* **2020**, *51*, 1874–1886. [\[CrossRef\]](#)
56. Stadler, F.; Antrekowitsch, H.; Fragner, W.; Kaufmann, H.; Uggowitz, P.J. The effect of main alloying elements on the physical properties of Al-Si foundry alloys. *Mater. Sci. Eng. A* **2013**, *560*, 481–491. [\[CrossRef\]](#)
57. Tian, L.; Anderson, I.E.; Riedemann, T.; Russell, A.M. Modeling the electrical resistivity of deformation processed metal-metal composites. *Acta Mater.* **2014**, *77*, 151–161. [\[CrossRef\]](#)
58. Li, L.F.; Li, D.Q.; Mao, F.; Feng, J.; Zhang, Y.Z.; Kang, Y.L. Effect of cooling rate on eutectic Si in Al-7.0Si-0.3Mg alloys modified by La additions. *J. Alloys Compd.* **2020**, *826*, 154206. [\[CrossRef\]](#)
59. Zhang, L.L.; Zheng, Q.J.; Jiang, H.X.; He, J.; Zhao, J.Z. Effect of La addition on microstructure evolution of hypoeutectic Al-6Si alloys. *J. Mater. Sci.* **2020**, *55*, 7546–7554. [\[CrossRef\]](#)
60. Qi, Z.Y.; Wang, B.; Jiang, H.X.; Zhang, H.; Li, B.; Zhai, G. Effect of trace rare earth La on microstructure and properties of Al-7Si-0.6 Fe alloy. *Acta Phys. Sin.* **2024**, *73*, 076401. [\[CrossRef\]](#)

Disclaimer/Publisher's Note: The statements, opinions and data contained in all publications are solely those of the individual author(s) and contributor(s) and not of MDPI and/or the editor(s). MDPI and/or the editor(s) disclaim responsibility for any injury to people or property resulting from any ideas, methods, instructions or products referred to in the content.